Catalysis Science & Technology

PAPER

View Article Online
View Journal | View Issue

Cite this: *Catal. Sci. Technol.*, 2024, **14**, 1336

Towards unconstrained catalyst shaping: high accuracy DLP printing of porous γ-Al_2O_3-based catalysts†

Luca Mastroianni,[ab] Vincenzo Russo,[ab] Kari Eränen,[a] Martino Di Serio,[b] Dmitry Yu. Murzin*[a] and Tapio Salmi[a]

3D printing, or additive manufacturing (AM), is one of the key technologies of the fourth industrial revolution (Industry 4.0) as it will transform the whole concept of manufacturing. AM enables rapid, sustainable and cost competitive production of highly complex designs. Applied to catalyst shaping, 3D printing paves the way for completely new architectures which have the potential to enhance mass transfer rates in shaped catalysts. Digital light processing (DLP) is a highly promising printing technology among the different 3D printing alternatives owing to excellent printing resolution and high printing speed. When applying DLP printing for ceramic materials, important catalyst requirements (such as the specific surface area) are often sacrificed to obtain mechanically stable parts. Herein, a novel methodology to DLP print γ-Al_2O_3 catalyst structures with a good mechanical stability and a high surface area is described. Introduction of active gold nanoparticles on the alumina supports was explored with different deposition methods and the catalytic activity was demonstrated in the oxidative dehydrogenation of bioethanol. The obtained results demonstrate a high potential of the method to remove all the constrains in catalyst shaping.

Received 16th November 2023,
Accepted 31st January 2024

DOI: 10.1039/d3cy01592k

rsc.li/catalysis

1. Introduction

The climate crisis that the mankind is experiencing today has been the driving force for the continuous research of new strategies to conduct fundamental chemical transformations. Catalysis, particularly heterogeneous catalysis carried out in the presence of solid materials, is one of the key fields of science in materializing the breakthrough of new technologies. Besides the nature of the catalytically active element, the catalyst shape and size are also of high importance as they strongly affect the production rates.[1] Very small catalyst particles are employed at the laboratory scale to minimize the retarding effect of the mass transfer on the observed chemical kinetics, but on a larger scale the presence of large catalyst pellets is important to control the pressure drop. Therefore, the transport of molecules towards the active sites controls the overall reaction rate in the large majority of the industrial-scale chemical processes.[2] Structured catalysts and reactors such as monoliths,[3] solid foams[4] and microreactors[5] have been developed in the last years to enhance local turbulence, thus improving fluid–solid mass transfer rates, and to minimize the diffusional path lengths, especially for microreactors and monoliths, where thin catalyst layers are applied. Recently, the breakthrough of 3D printing has opened completely new perspectives.

Known also as additive manufacturing, 3D printing has been established as a disruptive manufacturing technology 30 years ago as it enables inexpensive, rapid and reliable production of complex structures which are impossible to be shaped by conventional methods.[6] The technology is already massively used in many relevant sectors (*e.g.*, aerospace engineering, dentistry, art, and jewelry[7,8]) and it is expected to revolutionize chemical engineering in the near future with new concepts applicable on chemical reactors, heat exchangers and reactor internals.[9,10] In the last five years, a huge interest has grown in the possible implementation of 3D printing as a catalyst shaping technique.[11,12] The opportunities are rather clear to the eyes of chemical engineers: additive manufacturing unlock the possibility to govern the fluid flow within heterogeneous catalysts, because new architectures can be designed very precisely to meet the requirements of high mass and heat transfer rates combined with a low pressure drop. The process starts with the construction of a three-dimensional model with a computer aided design (CAD) software, which is generally converted

---

[a] *Laboratory of Industrial Chemistry and Reaction Engineering, Åbo Akademi University, FI-20500 Turku/Åbo, Finland. E-mail: dmurzin@abo.fi*
[b] *Università di Napoli "Federico II", Chemical Sciences Department, IT-80126 Napoli, Italy*

† Electronic supplementary information (ESI) available. See DOI: **https://doi.org/10.1039/d3cy01592k**

into a standard tessellation language (STL) file. Then, the digital design is sliced in several bidimensional layers and modified in numerical instructions (G-code) that the printer can elaborate.[13] Finally, the 3D printer builds the objects in a layer-by-layer fashion. Therefore, additive manufacturing allows the digital control of the catalyst architectures and fine tuning *via* topology optimization once the physics of the chemical system is known.[14]

As the majority of the industrial catalysts comprehend ceramic materials (*e.g.*, alumina, silica and zirconia) as the main component or the support of the active phase,[15] 3D printing of heterogeneous catalysts can be ascribed to the field of this science that concerns ceramic printing. Several technologies are nowadays available to accomplish the task: among them, direct ink writing (DIW) has been the most exploited because the existing technology on extrusion processes can be extended to additive manufacturing with this technique.[16] In DIW, a ceramic paste is extruded through needles to create the layers of the 3D structure. Binder jetting technologies (BJT) disperses droplets of liquid binding agent on a layer of ceramic powder and the process is repeated until completion of the 3D structure. Coarse particles are thus essential in BJT to guarantee efficient wetting of the binding ink and a successful print.[17] The technology is mature in the 3D printing of non-porous ceramics, and very recently it was successfully applied to produce solid structures with relevant porosity for the first time.[18] Both BJT and DIW technologies suffer from poor geometrical resolution, and the portfolio of 3D structures that can be successfully printed is limited.[12] All the geometrical constrains can be potentially removed using vat polymerization (VP) technologies. In VP printers, UV-light radiations trigger the localized polymerization of a photocurable resin comprising acrylate oligomers, a

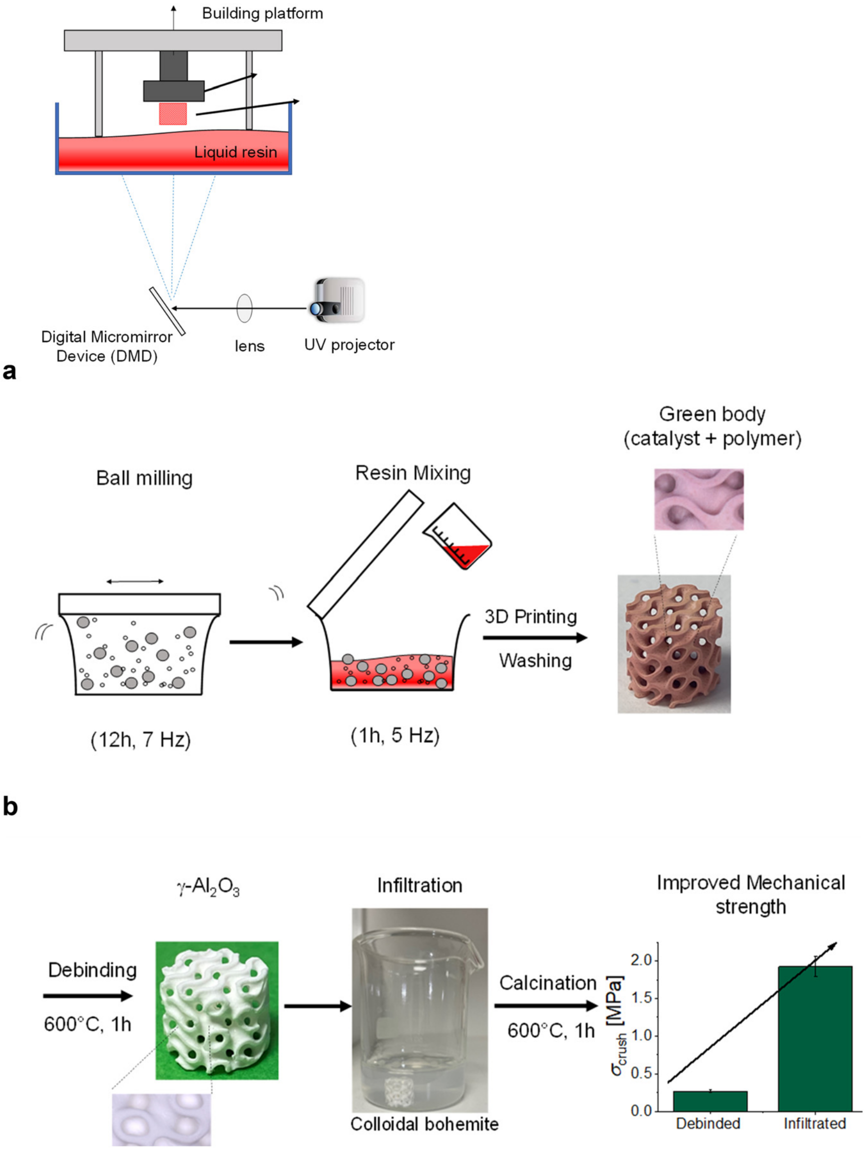

Fig. 1 a) Schematic representation of a DLP printer b) schematization of the printing policy.

photoinitiator (that generates the necessary radicals for the polymerization) and UV-light absorbers.[19] Modern VP printers enable to produce very precise features with resolutions up to 10 μm along the z direction,[20] ensuring improved freedom on the manufacturable designs. Depending on the UV-light source, three kinds of VP technologies are nowadays available: stereolitography (SLA) printers involve a UV laser to shape each layer while digital light processing (DLP) printers use a UV light projector to generate very precise cross sections of the 3D objects. In LCD printers, the UV light projector can generate superior image quality owing to the different illumination system of the projector *per se*. In classical "bottom-up" approaches, the shape is created on a transparent film, where the photosensitive resin is located, and the layer is cured on a building plate. As soon as the first layer is cured, the building plate moves up, allowing the liquid resin to replenish thus a subsequent layer can be created (Fig. 1a). DLP printers combine exceptional printing accuracy with a high-printing speed, making them suitable for a potential scale up.[21]

DLP printing of ceramics is possible by mixing the solid material in the powder form with the liquid resin. The resulting print, known also as "green body", comprises ceramic particles dispersed in the organic matrix. The polymer and organic additives are removed from the body with thermal energy in the so called "debinding" step. The heat treatment breaks the polymer chains, first in the constituent monomers and then into smaller units that are released from the green body as gaseous components. The debinding is a rather complex process, during which the risk of the defect formation is increasing.[22] Moreover, the mechanical strength reduces notably as the removal of the polymeric binder leaves the ceramic particles in a very weak contact. The consolidation of the ceramic particles in the 3D structure is usually enabled *via* thermal sintering at temperatures exceeding 1000 °C, which is nowadays a widely accepted method to ensure suitable mechanical properties of the final ceramic bodies.[23] Although enormous progress in 3D printing of non-porous materials such as alumina,[13,24,25] titania[26] and zirconia[27,28] has been made in the recent five years, the same approach is not applicable to obtain porous pellets relevant for catalysis, because thermal sintering destroys the internal porosity of the catalyst material, reducing dramatically the specific surface area.[29] Pyrolysis at a lower temperature is an option that preserves the catalyst porosity;[30] however, the presence of carbon deposits on the final structure can be detrimental for catalytic applications.

The goal of this work was to develop a new paradigm to DLP print pure γ-Al_2O_3 catalytic supports with suitable mechanical stability and a relevant surface area. Infiltration of colloidal particles of boehmite was adopted as a successful strategy to replace thermal sintering and preserve completely the catalyst porosity. Deposition of gold nanoparticles was conducted on the 3D structures, revealing the possibility to tune the location of the active metal within the 3D printed alumina architecture. The catalytic performance of the 3D printed structures was confirmed in the continuous transformation of bioethanol to valuable products. Moreover, the kinetic experiments revealed the decisive impact of the active metal location on the catalyst activity and product distribution.

2. Experiments and methods

2.1 Materials and methods

Polyethylene glycol diacrylate (PEGDA, M_n = 250 g mol^{-1}, Sigma Aldrich) was employed as the reactive olygomer, bis(2,4,6-trimethylbenzoyl)phenylphosphineoxide (IRGACURE 819, Sigma Aldrich) as the photoinitiator for the radical polymerization and Sudan III (Sigma Aldrich) as the UV-absorber. 1-Propanol (Sigma Aldrich) was used as a non-reactive diluent. The water dispersible boehmite Disperal P2 (Condea Chemie) was used as the precursor of γ-Al_2O_3 and Span80 (Sorbitan monooleate, Sigma Aldrich) was selected as the dispersant. In some formulations, attapulgite (GelEst) was employed as a clay binder to explore a potential improvement of the mechanical strength on the printed structures.

The DLP printer employed in this work was purchased from B9Creations. The building platform of the printer was 96 × 54 mm, while the maximum printing height was 127 mm. An industrial HD UV LED light engines was used as the light source with the wavelength of the UV-light of 405 nm. In all the prints, the layer thickness was set at 40 μm while and the exposure time to 6 seconds per layer, but the first six layers required a higher exposure (30 s) to ensure good adhesion of the printed part to the building plate. The computer designs displayed in this work were made using nTopology software, while B9Create 2.0 software was used to slice the STL files.

2.1.1 Resin preparation. The solid material (either pure boehmite or a mixture of boehmite and attapulgite) was dried at 110 °C in an oven for 6 h to remove the excess of moisture. Afterwards, it was introduced in a mixer mill (MM500, Retsch) together with 12 stainless steels balls (d = 1.5 cm) and it was ball milled for 15 h at 7 Hz. PEGDA, Sudan III and Span80 were subsequently introduced in the mixer mill and the mixing frequency decreased to 5 Hz. 1-Propanol was added in a sufficient amount (depending on the specific formulation) to obtain a suitable viscosity for 3D printing while maintaining a high solid-to-polymer ratio. The mixture was kept under mixing for 1 h to obtain a homogeneous suspension of the catalyst particles in the liquid polymeric matrix. Finally, the phototinitiator IRGACURE 819 was added to the resin and mixed at 3 Hz for two minutes. The solubilization of the photoinitiator was left at the end as premature polymerization of the resin was observed when it was added from the beginning, probably because of the high energy input during mixing in the milling unit.

2.1.2 Post processing. The printed objects were immersed in ethanol and exposed to ultrasound for five minutes to remove the excess of the liquid from the structures. The successful prints were subsequently placed in a B9 Model cure XL unit (B9 creations), where they were exposed to UV light for five minutes at 40 mW cm^{-2} and other five minutes at 70 mW cm^{-2} to complete the polymerization of possible uncured oligomers. Then, the samples were dried at 110 °C overnight to remove the excess of volatile components *i.e.*, ethanol and propanol. The green bodies were debinded at 600 °C for 1 h to remove the organic components from the solid mixture. The heating rate was set at 0.2 °C min^{-1} to ensure slow polymer degradation. The set point temperature was kept for 1 h to complete the thermolysis of the organic molecules, which was confirmed *via* quantification of the carbon content in the sample. The phase transformation of boehmite to γ-Al_2O_3 proceeded simultaneously at this temperature, however, it was not sufficient to ensure particle consolidation in the 3D printed structure, which appeared fragile after the debinding process.

The mechanical strength of the printed alumina was improved *via* infiltration of boehmite particles. A stable boehmite slurry was prepared by mixing the water dispersible boehmite (5 wt%) in deionized water for 30 min. Nitric acid was added in small amounts (0.4 wt%) to ensure the formation of a very stable colloidal solution. According to the supplier, the chemical attack produces very small boehmite agglomerates, with the sizes in the range 20–500 nm. The pH after preparation was 2.8, reaching a stable value of 3.4 after 48 hours. Therefore, the colloidal solution was prepared at least two days before its utilization, and it was observed to be suitable for infiltration for at least three months after its preparation.

The printed structures were immersed in the prepared solution for 30 min to ensure complete adhesion of the particles on the structures. The excess of the liquid was removed by gently blowing air into the channels of the catalyst structure. The samples underwent further calcination at 600 °C for 1 h to convert the infiltrated boehmite to γ-Al_2O_3. In this case, the heating rate was set at 5 °C min^{-1}. The overall 3D printing methodology, from the resin preparation to the final alumina catalyst, is illustrated in Fig. 1b.

2.2 Deposition of gold nanoparticles on the 3D printed alumina structures

Deposition of an active metal on the alumina supports was investigated by introducing gold nanoparticles as the reference metal. Two established deposition–precipitation methods were studied: deposition–precipitation with urea[31] (DPU) and ammonia[32] (DP) as deposition agents.

In the DPU method, $HAuCl_4$ and urea were dissolved in deionized water to reach the final concentrations of 2.5×10^{-4} and 0.21 M, respectively. Then, the solution was heated up at 80 °C to promote slow decomposition of urea and to control the deposition pH of the gold nanoparticles. In the DP method, the temperature was set at 70 °C and NH_3 was dosed every 0.5 h to increase stepwise the pH of the deposition solution. The selected pH values were 4.5, 6 and 8. In both methods, the total deposition time was 4 h. The 3D printed structures were attached on the blade of a stirrer with the Teflon tape before immersion in the solution and the stirring rate was adjusted to 350 rpm. At the end of the deposition procedure, the catalyst structures underwent washing with deionized water until chloride free performing $AgNO_3$ test to controlling the presence of chlorine in the washing solution. The samples were dried overnight at 50 °C and, afterwards, calcined at 300 °C for 3 h.

2.3 Characterization techniques

The particle size of the boehmite particles was evaluated using a Malvern Mastersizer 3000 laser diffractometer. The samples were dispersed in pure ethanol using a Hydro EV sample dispersion unit. Thermogravimetric analysis (TGA) was performed to analyse the decomposition profile of the organic matrix in the printed materials. Approximately 10 mg of sample was inserted in an aluminium cup and the weight loss was detected ranging from room temperature to 900 °C (heating rate 10 °C min^{-1}) under an air flow of 50 mL min^{-1}. The samples were dried overnight at 110 °C in an oven to remove the excess of propanol and humidity in the structure. Scanning electron microscopy (SEM/EDX, Leo Gemini 1530) micrographs were obtained to see the morphology of the printed samples on the micrometre scale. Inspections of the internal morphology and the element distribution were conducted immersing the samples in epoxy resin and grinding them with fine sandpaper to penetrate in surface without uncontrolled crushing. Nitrogen physisorption (Micromeritics 3 Flex 3500) was applied for the determination of surface areas and pore size distributions. Small monolithic structures (0.5 × 0.5 cm) were prepared to fit them in the measuring tube to conduct the measurements on the 3D printed samples avoiding crushing. The compressive strength was determined using an L&W crush tester with two parallel plates (SE 048, Lorentzen & Wettre, Sweden). The samples were placed vertically between the two plates, with one plate moving towards the other one at the rate of 50 mm s^{-1}. The crushing strength was obtained normalizing the force required to break the sample by the contact area of the samples with the plates. The reference printed structure for the tests was a monolithic structure with periodic rotation of the *xy* plane (Fig. 4). Therefore, the contact area takes into account the large cavities of the cross-section. X-ray diffraction (XRD) measurements were carried out using a PANalytical Empyrean diffractometer, operating with a Cu-K_α radiation source. The samples were crushed to powders and analysed of 2θ values of 10–90. The surface charge and the isoelectric point of the prepared alumina samples was determined using a Zetasizer Nano ZS (Malvern Instruments, United Kingdom) employing the light scattering technique while the potentiometric method (MPT-2) was applied for pH measurements. NaOH and HCl solutions were used to titrate pH of the suspension, which was varied from 3 to 10. The 3D

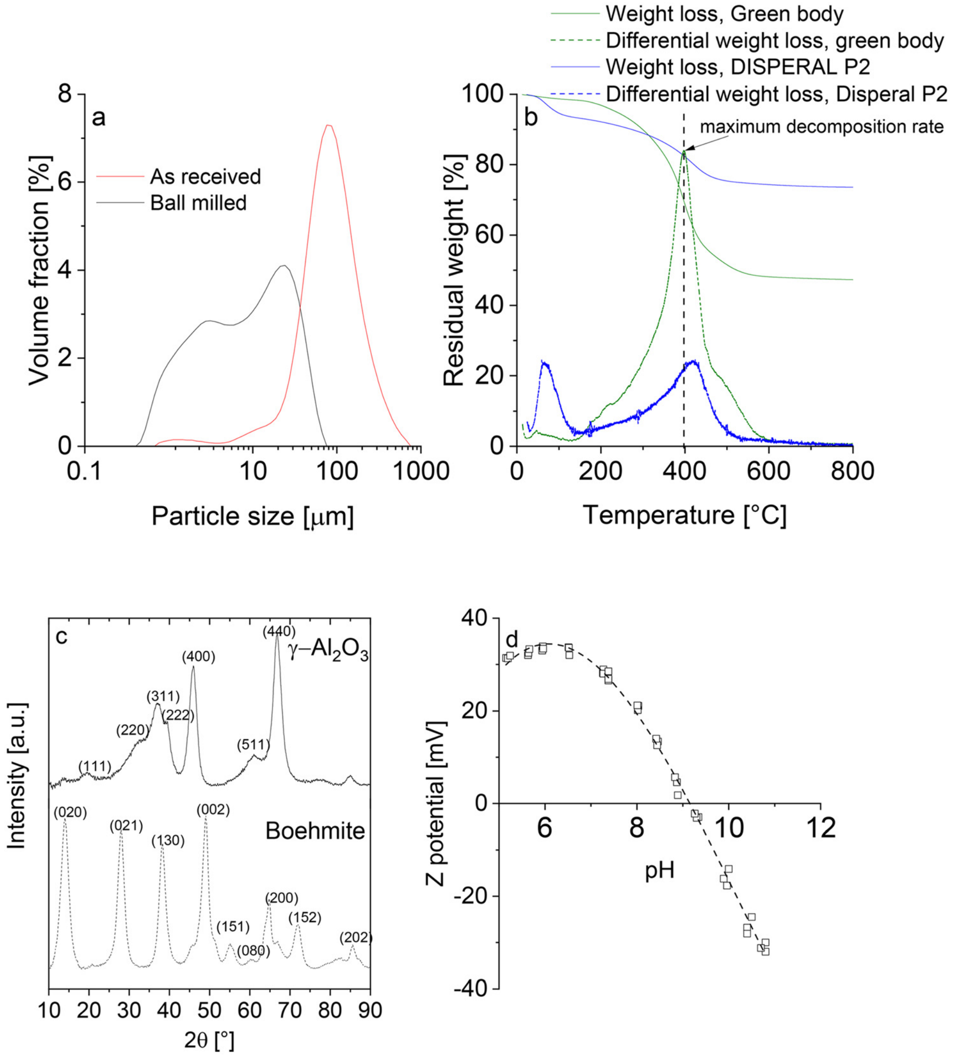

Fig. 2 a) Particle size distribution of boehmite b) thermogram of pure boehmite and the green body c) XRD profiles of boehmite and γ-Al_2O_3 d) zeta-potential as a function of pH for γ-Al_2O_3.

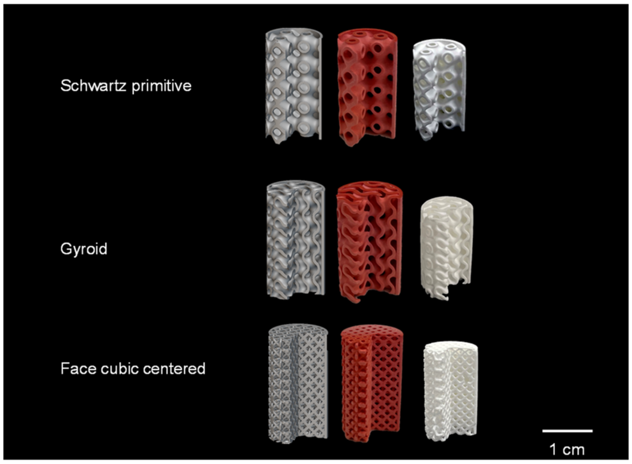

Fig. 3 Examples of 3D printed periodic structures to test the printing performance. Computer design in nTopology (left), green body (center) and final printed alumina (right).

printed samples were crushed in a mortar into powders prior to the measurements that were carried out at room temperature and 0.1 wt% solid concentration. The final curve was determined as an average of three subsequent measurements. Infrared spectroscopy (ATI Mattson – Infinity Series) with pyridine as the probe molecule was applied to quantify the Brønsted and Lewis acidities. The samples were crushed and pressed to obtain a thin catalyst pellet of approximately a weight of 14 mg. The sample was exposed to a pyridine flow for 30 min at 100 °C to ensure complete adsorption on the acid sites. IR measurements after the pellet treatment at 250, 350 and 450 °C were carried out at 100 °C to obtain quantitative information on the acid sites and their relative strengths. TEM (JEOL JEM-1400Plus) was applied to measure the Au nanoparticle distribution. The necessary particles for the measurements were obtained by scratching the surface of the structures. The measurements were repeated on three different samples for each deposition method.

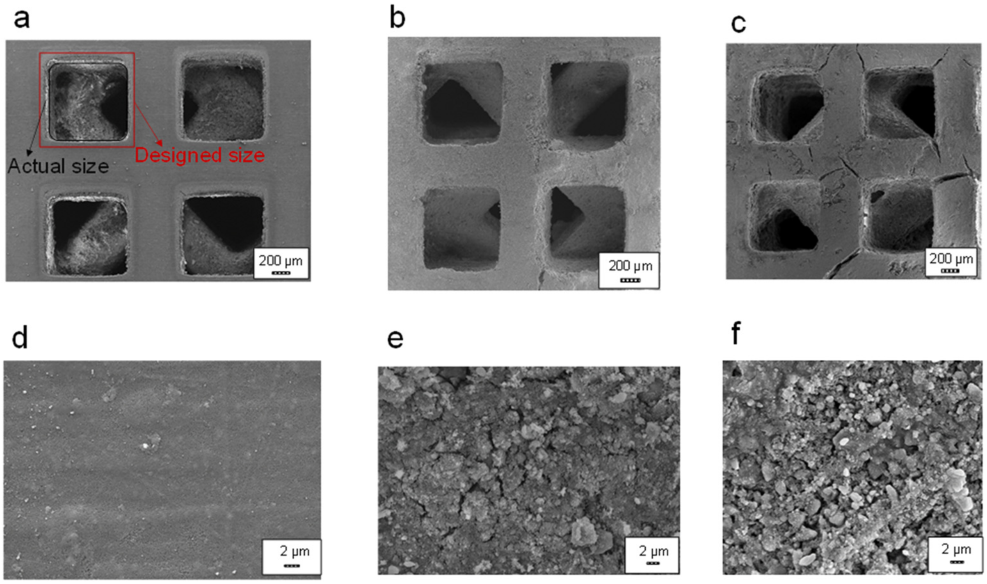

Fig. 4 SEM micrographs of the 3D printed green body (a and d), debinded (b and e) and infiltrated (c and f) γ-Al_2O_3 support.

2.4 Kinetic investigations

Catalytic activity of the 3D printed Au/Al_2O_3 and pure Al_2O_3 catalytic architectures (Fig. S5†) was tested in the continuous transformation of bioethanol to valuable products. The catalytic experiments were aimed to demonstrate the catalytic activity of the 3D printed structures and the influence of different gold deposition methods on both the catalytic activity and the product distribution. The observed reaction network was rather complex: along with oxidative dehydrogenation giving acetaldehyde as a product, mainly catalysed by gold nanoparticles, alumina-catalysed dehydration reactions appeared to form ethylene and diethyl ether simultaneously on the catalyst surface. Furthermore, total oxidation of acetaldehyde to CO_2 was detected at high ethanol conversion levels (Fig. S1a†). The schematic process flow diagram is displayed in Fig. S1b.† Neat ethanol was fed with a high precision HPLC pump at the desired flow rate and mixed with oxygen and helium before entering the tubular reactor. The mixture was heated up to the desired temperature in a 10 cm section of the reactor filled with inert glass sand before entering the catalytic zone, which comprised two 3D printed alumina structures with squared channels and periodic 90° rotation (every 1 mm) of the *xy* plane along the *z* direction. The diameter was set at 1.1 cm in the CAD design allowing the structure to fit into reactor tube (1 cm) after shrinking, while the length was set at 1 cm. The effluent from the reactor was analysed and quantified with an online GC. In all the experiments, the total volumetric flow rate was 100 mL min^{-1}, the oxygen-to-ethanol molar ratio was 1 and the ethanol partial pressure was 0.37 atm. All the experiments were carried out in isothermal conditions and the reaction temperature was varied from 200 °C to 275 °C.

3. Results and discussion

3.1 Resin properties

The particle size distribution of boehmite is shown in Fig. 2a. The ball milling step refined the particle size of the initial boehmite, which contained more than 90% of the particles exceeding the established layer thickness (40 μm). In classical applications of the DLP printing for ceramic materials, sub-micronic ceramic particles are employed to guarantee smooth printed layers, improving the particle packing in the green body and reducing shrinking caused by debinding and sintering.[33] A bimodal particle size distribution was recorded with a d_{90} value of 37 μm after ball-milling. As the resulting structures did not exhibit structural defects (Fig. 3), it can be concluded that the fraction of particles with the size bigger than the layer thickness can be very well tolerated in DLP printing of ceramics.

Formulations in which only the essential components (the polymer, the photoinitiator and the boehmite) were present produced uncontrolled polymerization in the liquid resin because of the severe light scattering introduced by the solid particles[19] (Fig. S2a†). This negative effect was successfully mitigated adding the colorant SUDAN III in the mixture, which acts as a UV light absorber controlling the light pathway in the liquid matrix. Although the addition was extremely small (0.15 wt%), it considerably improved the quality of the 3D prints (Fig. 3 and S2b†).

The solid amount in the ceramic resin is of high importance as the polymer material must be removed from the structure once the manufacturing process is completed. When the solid content was too low, cracks and delamination appeared in the final structure after the polymer burnout because of the heavy weight loss in the structure. Formulations with solid loadings less than 40 wt% were successfully printed but the structure collapsed after the polymer debinding (Fig. S2c†).

While high catalyst-to-polymer ratios are essential to retain the structural integrity after the removal of the organic components, they are detrimental for the printability of the ceramic resin. High solid loading inevitably results in an increase of viscosity, preventing the liquid resin to flow where the printing proceeds. A classical failure that appeared when preparing viscous formulations is displayed in Fig. S2d.† An empty circle was formed where the layers were polymerised, because the 3D print was stopped as the resin was locally cured, and new liquid resin was unable to flow to replenish the printing area. Moreover, some objects also detached from the building plate because of the high stress caused by the suction forces as the building plate was lifted in a viscous medium. It was found that addition of propanol as a non-reactive diluent was of crucial importance to maintain an acceptable level of viscosity while having a sufficiently high catalyst-to-polymer ratio during the 3D shaping process. It is worth to mention that the solvent evaporation became an issue after 1.5 h of printing regardless of a high boiling point of propanol. Hence, structures with a height exceeding 2 cm were not printed efficiently with the adopted printing program. To overcome this issue, wetting agents (*e.g.*, glycerol) might be applied to create hydrogen bonds with propanol thus preventing its evaporation. Alternatively, it is possible on some DLP printers to stop the printing process at a certain moment in time. In this way, some propanol can be added to the mixture, the resin can be mixed until sufficient viscosity and, finally, the printing can start again.

Drying at 110 °C enabled preliminary evaporation of propanol prior to debinding. A similar approach was previously proposed using ethanol as the diluent.[29,34] However, a visible change of the resin viscosity can be experienced during 3D printing because of the low boiling point of ethanol. Eventually, the optimal resin had a 60 wt% content with respect to the organic matrix (the sum of oligomers and other additives) as a good compromise between a suitable viscosity for adequate printing and structural stability after thermolysis. The dispersant concentration was 3 wt% with respect to the boehmite mass. The concentrations of SUDAN III and the photoinitiator were 0.15 and 1 wt%, respectively. The final content of 1-propanol in the resin was 18 wt%; therefore, the actual loading of boehmite in the ceramic resin used in the 3D print was 49 wt%.

Besides printability and structural integrity, the presence of solid particles in a ceramic resin is responsible for a significant decrease of resolution because of the inevitable light scattering and polymerization outside the designed voxels.[35] Although addition of a UV absorber mitigated this phenomenon, a discrepancy between the size defined by the CAD design and the actual size was inevitably observed. To quantify the effect, analysis was conducted for 3D monolithic structures designed with the squared channels size of 1.2 mm and the spacing between channels of 0.3 mm. SEM micrographs of the green body (Fig. 4a) confirmed that the actual channel dimension is reduced by 18% (990 μm) because of polymer overcuring. Hence, the spacing between channels became higher (550 μm). The total overcuring effect overcame the shrinking caused by the propanol evaporation, which was found to be *ca.* 3%. Quantitative information about overcuring is of crucial importance for the correct and precise design of the catalytic architecture of interest.

3.2 Post processing

The obtained thermograms displaying the relative differential weight losses are shown in Fig. 2b. The degradation of the organic polymers occurred in the temperature range 180–600 °C, with a maximum in the decomposition rate at 400 °C. Within this temperature window, two mechanisms governed the mass loss *i.e.*, i) degradation of the acrylate polymer into smaller units and ii) complete volatilization of the organic molecules, which were mainly converted into CO, CO_2, and light hydrocarbons.[22] The thermogram served as an instruction to define the thermolysis program, particularly the final temperature and the heating rate. Besides the organic matrix decomposition, other processes took place simultaneously during debinding process, namely mass transport of the gaseous product through the porous network, interactions of these species with the ceramic body, changes in the organic binder distribution within the structure and shrinkage of the 3D shaped object.[22] All these processes could eventually result in an inadequate debinding with cracks and deformations in the final structure. Hence, the heating rate was kept low (0.2 °C min^{-1}) minimizing the risk of structural failures during the weight loss. The final temperature (600 °C) was kept for 1 h to ensure complete volatilization of the organic molecules. CHNS (carbon, hydrogen, nitrogen, sulfur) analysis confirmed that the carbon content in the printed catalyst was 0.5 wt% only. The final weight was lower than the nominal boehmite content (60 wt%) in the resin as the transformation the boehmite to γ-alumina and subsequent removal of water in the solid lattice occurred at these temperatures. In terms of the size reduction during debinding, the radial and axial linear shrinkages were measured to be 10% without any significant differences between different architectures.

The final temperature of 600 °C was not sufficient to ensure the consolidation of the ceramic particles in the 3D structure. The resulting shaped alumina supports were extremely fragile, showing a poor mechanical stability. Addition of the clay binder in different amounts in the formulation did not improve the mechanical strength significantly. In numerical terms, the compressive strength was always less than 0.4 MPa. The SEM micrographs of the printed alumina–attapulgite (Fig. S3†) samples showed that the two phases were only mechanically mixed without forming a network needed for an improvement of the mechanical strength. Therefore, it can be concluded that the classical methods to improve the strength in extrusion *i.e.*, by addition of clay binders, are not helpful in the DLP printing of catalyst supports. The applied pressure on the ceramic paste in the catalyst shaping by extrusion produces interphases between the catalyst particles and the clay binder which are proven to be beneficial for the mechanical properties of the final extrudates.[36,37] When utilizing a DLP printer, the shaping occurs *via* UV radical polymerization without any external pressure, explaining absence of a network between the catalyst and the binder. As a result, the printed supports appeared weak after the polymer debinding. Thermal sintering is the simplest method to establish a rigid network between the alumina particles and to improve the mechanical properties of the final ceramic shape, but this approach is detrimental for catalytic applications as it destroys the porosity of the catalyst reducing dramatically the surface area. In addition, the phase transformation from the γ- to the non-porous α-alumina phase occurs at temperatures exceeding 800 °C.[38]

Therefore, infiltration of boehmite particles was proposed as an innovative method to improve the mechanical stability. The green body *i.e.*, the composite alumina + polymer showed excellent mechanical properties, with a compressive strength of 50 MPa. The mechanical properties were completely lost after polymer thermolysis as proven by the low value of the compressive strength (0.3 MPa). Simple immersion in the colloidal boehmite suspension determined a seven-fold increase (2 MPa) of the compressive strength, without any further significant improvement after subsequent calcination of the infiltrated boehmite to γ-alumina. Although the value is lower than the one of the green body, the mechanical strength was sufficient for further catalyst processing *i.e.* gold deposition under stirring in the liquid precursor, packing of the reactor and catalytic experiments *per se*.

The mass increase after the impregnation with the colloidal boehmite was 3 wt% only, nonetheless the final properties were clearly enhanced. The SEM micrographs obtained at different steps of the printing procedure are displayed in Fig. 4. The green body appeared non-porous as presence of polymer is substantial (Fig. 4a and d). Removal of the organic matrix leaves the structure rather weak, with several non-homogeneities left from the polymer burnout (Fig. 4b and e). The colloidal particles filled the empty spaces left from the organic molecules and the structure became harder (Fig. 4c and f). Some fractures appeared on the sample surface after the infiltration because of the high vacuum applied in the SEM instrument. However, they were not observed when analysing the samples with the optical microscope. As the weight increase after infiltration was small, the particle infiltration occurred exclusively on the external surface.

Table 1 summarizes the specific surface areas and the pore volumes at different steps of the printing procedure. A decline of the surface area of boehmite in the powder form was the result of the phase transformation and the crystal lattice reconstruction.[39] The adsorption isotherm was of H2 type for both the boehmite and alumina (Fig. S4a†) but larger pores, in the classical dimension range for mesoporous materials, were observed in the alumina (Fig. S4b†), leading to an increase of the total pore volume, which is generated only by mesopores as contribution of other type of porosity was marginal (Fig. S4b†) thus confirming the mesoporous nature of alumina. The infiltration process did not alter substantially the total surface area of the structures with respect to the calcined powder, confirming the potential of the proposed method to retain relevant textural properties in the shaped catalysts. Thus, this work defined a starting point to obtain highly porous and mechanically stable 3D printed catalyst architectures with unprecedented resolution.

Table 1 Surface area and pore volume at different steps of the printing procedure

Material	Morphology	Surface area $m^2\ g^{-1}$	Pore volume $cm^3\ g^{-1}$
Boehmite	Powder	218	0.23
γ-Al_2O_3	Powder	173	0.28
	3D printed, debinded	168	0.27
	3D printed, infiltrated	150	0.27

3.3 Alumina identification

The XRD profiles before and after the heat treatment are shown in Fig. 2c. The pattern of the alumina precursor matches well with the diffractograms of boehmites found in the existing literature.[40] Similarly, the XRD diffractogram of the resulting alumina after debinding at 600 °C can be unequivocally attributed to metastable alumina. Although it is straightforward to differentiate between transition and thermodynamically stable alumina phases, the discrimination between meta-stable aluminas is more challenging.[18] The decomposition products that are expected to be formed during the calcination at 600 °C of aluminium hydroxides are γ- and η-Al_2O_3, which are obtained starting either from boehmite or bayerite, respectively.[41] Small differences in tetragonal deformation and oxygen lattice order are the main discriminating factors of the two transition phases.[38] Tsybulya and Kryukova have suggested that the main differences between the XRD spectra of γ- and η-Al_2O_3 are in the (111) diffraction peak, which is sharper in η-Al_2O_3, and in a small shift of the (311) peak to smaller angles for γ-Al_2O_3 because of the pronounced tetragonal distortion.[41] The peak (440) might appear splitted or shouldered in disordered γ-Al_2O_3 phases which are typically obtained after heat treatment at temperatures less than 600 °C.[42] The absence of a sharp (222) peak indicates a low oxygen sublattice order.[43] Based on the applied alumina precursor and XRD information, the sample should mainly consist of γ-Al_2O_3, but a fraction η-Al_2O_3 might also coexist in the calcined samples.

The zeta potential as a function of the pH is shown in Fig. 2d. The point of zero charge of 9.1 falls in the upper bound of values previously found for γ-Al_2O_3. The isoelectric point is typically dependent on the history of the sample as well as on crystallography. Such a high value of the zeta potential indicates a strong presence of surface hydroxylation generating a positive surface charge within a broad range of pH.[44] Pyridine-FTIR measurements confirmed the Lewis acidic nature of the alumina surface (Table 2). The total amount of Lewis acid sites was 27 μmol g^{-1}, with 18 μmol g^{-1} of weak and 9 μmol g^{-1} of medium sites, while Brønsted acidity was not detected.

3.4 Gold deposition

Remarkable differences in both the gold nanoparticle size and the spatial distribution within the catalyst structure were observed when employing the different deposition methods. The distribution of gold along the axial coordinate was visually explored by scratching the surface with a metallic spatula. The clear difference in the colour suggested that gold was only deposited on the outer surface when using the DPU method (Fig. S5a†), while it was evenly distributed when applying the DP method (Fig. S5b†). Quantitative information about the gold distribution was obtained by investigating the samples at a certain cross section with a low brightness level, so that only the heaviest atoms (gold) scatter sufficiently the electron beam to appear brighter. The micrographs confirmed that gold was present on the outer catalyst shell only when applying the DPU method (Fig. 5a), while a more homogeneous distribution appeared with the DP method (Fig. 5b). The EDX scans along a specific channel wall determined that the gold layer was 50 μm in case of the DPU method (Fig. 5c). Different nature of the gold complexes in the deposition process might justify such behaviour during the deposition. When using ammonia to control the pH, gold is mainly deposited in the form of $Au(OH)_3$ or chloro–hydroxy complexes, $[AuCl(OH)_3]^-$ and $[AuCl_2(OH)_2]^-$ depending on the applied pH. Moreover, the anion can be formed *via* a direct interaction with ammonia.[45] On the other hand, gold(III) interacts with the products of the urea decomposition *e.g.*, hydroxyl and isocyanate anions, changing the nature of the nucleation sites and the final composition of the precipitated gold, which has been acknowledged to be an amorphous compound originated from the precipitating agent.[46] The presence of different precursors and thus different speciation of gold in the liquid phase resulted in different penetration of gold in the porous structure of alumina. The ICP measurements revealed that the deposition efficiency of both methods was the same (75%) and the final gold loading was 1.5 wt%. TEM micrographs confirmed that the density of nanoparticles was high in the catalysts prepared with the DPU method as the gold nanoparticles were extremely close to each other (Fig. 5e), which is not the case of the catalysts prepared with the DP method (Fig. 5f). The nanoparticle size distribution was narrower, and the particles were smaller in the urea-deposited gold, which is counterintuitive as the active site density was larger. Reasonably, different gold precursors have different aurophilicities affecting the growth mechanism and different mobilities on the surface, explaining the different particle size distribution when different precipitating agents are utilized.[45]

Table 2 Acidity of neat alumina and gold on alumina catalysts prepared with different deposition methods

Material	Lewis acidity, μmol g^{-1}			
	Weak	Medium	Strong	$\sum$
Al_2O_3	18	9	0	27
Au/Al_2O_3, DPU method	24	2	0	26
Au/Al_2O_3, DP method	31	4	0	35

3.5 Kinetic results and discussion

The results of the kinetic investigations are summarized in Fig. 6. Overall, the catalysts were stable over 70 h of experiments, meaning that the structures were stable and no sintering took place under the imposed experimental conditions (Fig. S6†). In general terms, the experiments successfully proved catalytic activity of the 3D printed catalysts as remarkable conversion levels (>60%) were observed already at 250 °C (Fig. 6a). The turnover frequency (TOF) values ranged from 0.2 to 1.3 s^{-1}, being well in line with the values obtained for the same reaction on Au/Al_2O_3 catalysts in powder form.[47,48] Substantial differences appeared when comparing the neat alumina and the gold supported catalysts. Diethyl ether was the main reaction product when carrying out the reaction on γ-Al_2O_3 (Fig. 6b) since condensation of two molecules of ethanol requires Lewis acid sites.[49] Similar catalytic activity was observed for the Au/Al_2O_3 catalyst prepared with the DPU method within the entire temperature range (Fig. 6a) while the product distribution changed substantially, because the presence of gold nanoparticles promoted the oxidative dehydrogenation of ethanol to acetaldehyde (Fig. 5b and c).[50] Therefore, selectivity towards acetaldehyde was clearly enhanced by the presence of gold nanoparticles. The Au/Al_2O_3 catalyst prepared with the DP method showed the best catalytic activity, with a conversion close to unity already at 250 °C (Fig. 6a). The product distribution shifted considerably towards the selective oxidation product, acetaldehyde at low conversion levels (Fig. 6c) and dependence of selectivity on conversion is in complete agreement with previous studies on a similar catalyst carried out in a microreactor unit.[5] On this catalyst, formation of diethyl ether was almost completely suppressed (Fig. 6b) but, at the same time, ethanol dehydration to form ethylene appeared as a significant side reaction.

The results showed that it is possible to drive chemical processes on 3D printed catalytic architectures with an appropriate selection of the deposition method for the active material. As the gold nanoparticles were dispersed on the external surface of the alumina support (DPU method), the

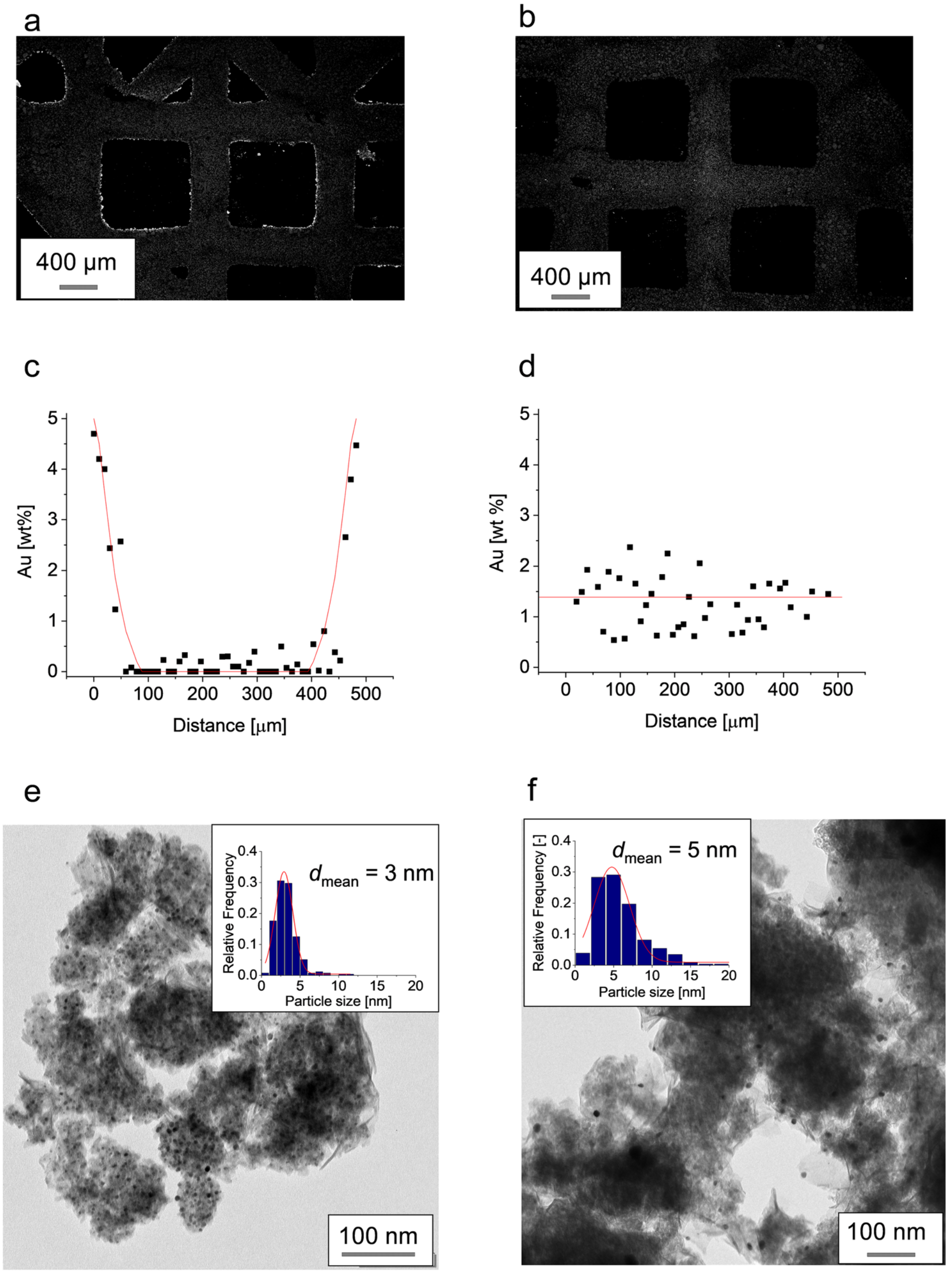

Fig. 5 Internal SEM micrographs of the 3D printed Au/Al_2O_3 catalyst prepared with a) DPU and b) DP method. EDX scans of the catalyst prepared with c) DPU and d) DP method. TEM micrographs and gold nanoparticle size distribution obtained with e) DPU and f) DP methods.

selectivity to acetaldehyde was only partially enhanced as ethanol encountered mainly the Lewis acid sites of the alumina support when diffusing inside the catalyst pore structure promoting dehydration reactions. This is detrimental for acetaldehyde formation, but the possibility to tune the vicinity and distribution of the active sites of different species can give substantial benefits for catalytic processes requiring bifunctional catalysts. The even distribution of gold (DP method) substantially enhanced the oxidation properties as gold nanoparticles were available within the porous structure. In addition, different selectivity to the acid-catalysed products (*i.e.*, ethylene, and diethyl ether) allows to suggest that explored deposition methods changed the nature of acidic sites of alumina.[51,52] Carrier *et al.* have pointed out that morphological changes of γ-Al_2O_3 phase might occur in aqueous solutions at pH ≥ 4 at sufficiently high contact times.[53] Therefore, the surface structure of alumina might be modified during the metal deposition thus changing the acidic properties of the support. FTIR measurements confirmed an increased amount of acid sites after deposition of gold *via* the DP method (Table 2). However, such variation is not substantial and cannot be regarded as the only descriptor in the shift of selectivity towards different dehydration products. The

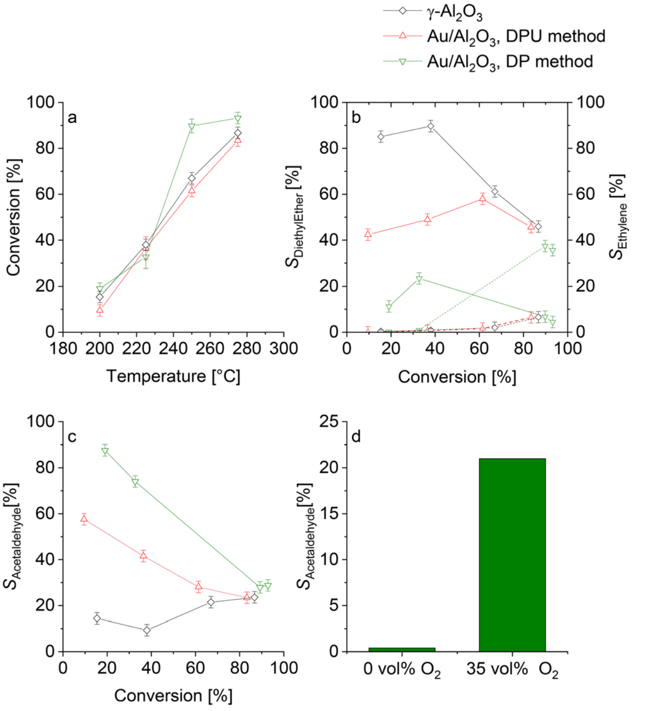

Fig. 6 Oxidative dehydrogenation of ethanol at atmospheric pressure, ethanol-to-oxygen ratio of 2 and flow rate of 100 mL min^{-1}. a) Ethanol conversion as a function of temperature b) selectivity towards the dehydration products *vs.* ethanol conversion (solid line is diethyl ether, dashed line is ethylene) c) selectivity to acetaldehyde *vs.* conversion d) selectivity to acetaldehyde in the presence and absence of O_2 on γ-Al_2O_3.

presence of electrophilic gold clusters on the alumina surface might have also affected the reactivity of alumina.[5] Finally, the presence of impurities (*e.g.*, chlorine and isocyanates) coming from different precursors could have also played a crucial role.

4. Conclusions

The potential of the high resolution DLP printing was exploited to create a new procedure for the design, manufacturing, and application of catalyst structures with a high geometrical complexity. It was demonstrated that the existing knowledge to DLP print ceramic resins can be applied to shape catalytic supports (herein, alumina) with hierarchical architectures designed to guarantee efficient local turbulence. Washcoating of colloidal particles was explored as an alternative post-processing method to improve the mechanical stability preserving the internal catalyst porosity, which is typically destroyed in the conventional thermal sintering. The proposed approach forms a new paradigm for further development of the 3D printing methodology, which requires substantial research efforts from the scientific community to meet the requirements for industrial catalysts. It was also demonstrated that deposition of active metal nanoparticles is possible and the distribution within the support can be governed by an appropriate selection of the deposition method. The kinetic experiments of alcohol oxidation proved catalytic activity of the 3D printed objects, with remarkable differences between the investigated techniques of the metal introduction. The results reflected the importance of proper deposition methods to drive selectivity of a given chemical process. The general outcome of this work encourages a further scientific development of the technique that can potentially lead to revolutionary process intensification. The applications are expected to be vast: not only for gas phase processes, but more importantly for catalytic three phase systems, where the intimate contact between the phases is still a challenge. For these systems, the modern topology optimization tools could enable the design of the optimal shapes to improve the flow properties at different scales, from the single 3D printed catalyst pellet to the chemical reactor, and the geometry to be realized by DLP printing technology.

Conflicts of interest

There are no conflicts to declare.

Acknowledgements

This work is part of the activities financed by the Academy of Finland through the Academy Professor grants 319002, 320115, 345053 (Tapio Salmi, Luca Mastroianni). Economic support from Åbo Akademi University Graduate School (Luca Mastroianni) is gratefully acknowledged.

References

1 S. Afandizadeh and E. A. Foumeny, Design of packed bed reactors: guides to catalyst shape, size, and loading selection, *Appl. Therm. Eng.*, 2001, **21**, 669–682.

2 D. Y. Murzin, *Chemical Reaction Technology*, De Gruyter, 2015.

3 E. Tronconi, G. Groppi and C. G. Visconti, Structured catalysts for non-adiabatic applications, *Curr. Opin. Chem. Eng.*, 2014, **5**, 55–67.

4 G. Araujo-Barahona, K. Eränen, J. P. Oña, D. Murzin, J. García-Serna and T. Salmi, Solid Foam Ru/C Catalysts for Sugar Hydrogenation to Sugar Alcohols-Preparation, Characterization, Activity, and Selectivity, *Ind. Eng. Chem. Res.*, 2022, **61**, 2734–2747.

5 L. Mastroianni, Z. Vajglová, K. Eränen, M. Peurla, M. Di Serio, D. Yu. Murzin, V. Russo and T. Salmi, Microreactor technology in experimental and modelling study of alcohol oxidation on nanogold, *Chem. Eng. Sci.*, 2022, **260**, 117920.

6 O. Santoliquido, G. Bianchi, P. Dimopoulos Eggenschwiler and A. Ortona, Additive manufacturing of periodic ceramic substrates for automotive catalyst supports, *Int. J. Appl. Ceram. Technol.*, 2017, **14**, 1164–1173.

7 T. Singh, S. Kumar and S. Sehgal, 3D printing of engineering materials: A state of the art review, *Mater. Today: Proc.*, 2020, **28**, 1927–1931.

8 A. Dawood, B. M. Marti, V. Sauret-Jackson and A. Darwood, 3D printing in dentistry, *Br. Dent. J.*, 2015, **219**, 521–529.

9 C. Parra-Cabrera, C. Achille, S. Kuhn and R. Ameloot, 3D printing in chemical engineering and catalytic technology: Structured catalysts, mixers and reactors, *Chem. Soc. Rev.*, 2018, **47**, 209–230.

10 L. Fratalocchi, G. Groppi, C. G. Visconti, L. Lietti and E. Tronconi, Adoption of 3D printed highly conductive periodic open cellular structures as an effective solution to enhance the heat transfer performances of compact Fischer-Tropsch fixed-bed reactors, *Chem. Eng. J.*, 2020, **386**, 123988.

11 E. Bogdan and P. Michorczyk, 3d printing in heterogeneous catalysis—the state of the art, *Materials*, 2020, **13**, 1–23.

12 J. Zhu, P. Wu, Y. Chao, J. Yu, W. Zhu, Z. Liu and C. Xu, Recent advances in 3D printing for catalytic applications, *Chem. Eng. J.*, 2022, **433**, 134341.

13 O. Santoliquido, F. Camerota, M. Pelanconi, D. Ferri, M. Elsener, P. D. Eggenschwiler and A. Ortona, Structured alumina substrates for environmental catalysis produced by stereolithography, *Appl. Sci.*, 2021, **11**, 8239.

14 C. B. Dilgen, S. B. Dilgen, D. R. Fuhrman, O. Sigmund and B. S. Lazarov, Topology optimization of turbulent flows, *Comput. Methods Appl. Mech. Eng.*, 2018, **331**, 363–393.

15 D. Y. Murzin, *Engineering Catalysis*, De Gruyter, 2020.

16 Q. Chen, E. Tian, Y. Wang, J. Mo, G. Xu and M. Zhu, Recent progress and perspectives of Direct Ink Writing applications for mass transfer enhancement in gas-phase adsorption and catalysis, *Small Methods*, 2023, **7**, 2201302.

17 X. Lv, F. Ye, L. Cheng, S. Fan and Y. Liu, Binder jetting of ceramics: Powders, binders, printing parameters, equipment, and post-treatment, *Ceram. Int.*, 2019, **45**, 12609–12624.

18 H. M. Bui, R. Fischer, N. Szesni, M. Tonigold, K. Achterhold, F. Pfeiffer and O. Hinrichsen, Development of a manufacturing process for Binder Jet 3D printed porous Al2O3 supports used in heterogeneous catalysis, *Addit. Manuf.*, 2022, **50**, 102498.

19 D. M. Shah, J. Morris, T. A. Plaisted, A. V. Amirkhizi and C. J. Hansen, Highly filled resins for DLP-based printing of low density, high modulus materials, *Addit. Manuf.*, 2021, **37**, 101736.

20 H. Goodarzi Hosseinabadi, D. Nieto, A. Yousefinejad, H. Fattel, L. Ionov and A. K. Miri, Ink material selection and optical design considerations in DLP 3D printing, *Appl. Mater. Today*, 2023, **30**, 101721.

21 K. Zhang, R. He, G. Ding, C. Feng, W. Song and D. Fang, Digital light processing of 3Y-TZP strengthened ZrO2 ceramics, *Mater. Sci. Eng., A*, 2020, **774**, 138768.

22 O. Santoliquido, F. Camerota and A. Ortona, The influence of topology on DLP 3D printing, debinding and sintering of ceramic periodic architectures designed to replace bulky components, *Open Ceram.*, 2021, **5**, 100059.

23 O. Santoliquido, G. Bianchi, P. Dimopoulos Eggenschwiler and A. Ortona, Additive manufacturing of periodic ceramic substrates for automotive catalyst supports, *Int. J. Appl. Ceram. Technol.*, 2017, **14**, 1164–1173.

24 Y. Zeng, L. Sun, H. Yao and J. Chen, Fabrication of alumina ceramics with functional gradient structures by digital light processing 3D printing technology, *Ceram. Int.*, 2022, **48**, 10613–10619.

25 L. Sun, P. Dong, Y. Zeng and J. Chen, Fabrication of hollow lattice alumina ceramic with good mechanical properties by Digital Light Processing 3D printing technology, *Ceram. Int.*, 2021, **47**, 26519–26527.

26 J. Guo, Y. Zeng, P. Li and J. Chen, Fine lattice structural titanium dioxide ceramic produced by DLP 3D printing, *Ceram. Int.*, 2019, **45**, 23007–23012.

27 D. A. Komissarenko, P. S. Sokolov, A. D. Evstigneeva, I. V. Slyusar, A. S. Nartov, P. A. Volkov, N. V. Lyskov, P. V. Evdokimov, V. I. Putlayev and A. E. Dosovitsky, DLP 3D printing of scandia-stabilized zirconia ceramics, *J. Eur. Ceram. Soc.*, 2021, **41**, 684–690.

28 J. Sun, J. Binner and J. Bai, 3D printing of zirconia via digital light processing: optimization of slurry and debinding process, *J. Eur. Ceram. Soc.*, 2020, **40**, 5837–5844.

29 H. Wang, P. Wang, Q. Wang, R. Zhang and L. Zhang, Preparation of a high-precision gamma-Al2O3 structured catalyst by DLP 3D direct printing for hydrogen production from methanol, *Ind. Eng. Chem. Res.*, 2021, **60**, 13107–13114.

30 Y. Wu, J. He, W. Huang, W. Chen, S. Zhou, X. She, W. Zhu, F. Huang, H. Li and H. Xu, Stereolithography 3D printed monolithic catalyst for highly efficient oxidative desulfurization of fuels, *Fuel*, 2023, **332**, 126021.

31 S. Franz, N. D. Shcherban, I. L. Simakova, M. Peurla, K. Eränen, J. Wärnå, T. Salmi and D. Y. Murzin, Oxidation of glucose and arabinose mixtures over Au/Al2O3, *React. Kinet., Mech. Catal.*, 2021, **132**, 59–72.

32 O. Reinsdorf, C. Pellegrin, C. Schmidt, M. Alvear, K. Eränen, D. Y. Murzin and T. Salmi, Selective oxidation of glucose using hydrogen peroxide as an oxidant: On the structure sensitivity of the apparent activation energy, *ChemCatChem*, 2023, **15**, 202300536.

33 O. Santoliquido, F. Camerota, A. Rosa and A. Ortona, A novel device to simply 3D print bulk green ceramic components by stereolithography employing viscous slurries, *Open Ceram.*, 2021, **5**, 100089.

34 G. Varghese, M. Moral, M. Castro-García, J. J. López-López, J. R. Marín-Rueda, V. Yagüe-Alcaraz, L. Hernández-Afonso, J. C. Ruiz-Morales and J. Canales-Vázquez, Fabricación y caracterización de cerámicas medinate impresión 3D DLP de bajo coste, *Bol. Soc. Esp. Ceram. Vidrio*, 2018, **57**, 9–18.

35 T. Zheng, W. Wang, J. Sun, J. Liu and J. Bai, Development and evaluation of Al2O3–ZrO2 composite processed by digital light 3D printing, *Ceram. Int.*, 2020, **46**, 8682–8688.

36 S. Y. Devyatkov, A. Al Zinnurova, A. Aho, D. Kronlund, J. Peltonen, N. V. Kuzichkin, N. V. Lisitsyn and D. Y. Murzin, Shaping of sulfated zirconia catalysts by extrusion: Understanding the role of binders, *Ind. Eng. Chem. Res.*, 2016, **55**, 6595–6606.

37 Z. Vajglová, N. Kumar, P. Mäki-Arvela, K. Eränen, M. Peurla, L. Hupa and D. Y. Murzin, Effect of binders on the

physicochemical and catalytic properties of extrudate-shaped beta zeolite catalysts for cyclization of citronellal, *Org. Process Res. Dev.*, 2019, **23**, 2456–2463.

38 R.-S. Zhou and R. L. Snyder, Structures and transformation mechanisms of the η, γ and θ transition aluminas, *Acta Crystallogr., Sect. B: Struct. Sci.*, 1991, **47**, 617–630.

39 M. Nguefack, A. F. Popa, S. Rossignol and C. Kappenstein, Preparation of alumina through a sol-gel process. Synthesis, characterization, thermal evolution and model of intermediate boehmite, *Phys. Chem. Chem. Phys.*, 2003, **5**, 4279–4289.

40 Y. Zheng, J. Song, X. Xu, M. He, Q. Wang and L. Yan, Peptization mechanism of boehmite and its effect on the preparation of a fluid catalytic cracking catalyst, *Ind. Eng. Chem. Res.*, 2014, **53**, 10029–10034.

41 S. V. Tsybulya and G. N. Kryukova, Nanocrystalline transition aluminas: Nanostructure and features of X-ray powder diffraction patterns of low-temperature Al2O3 polymorphs, *Phys. Rev. B: Condens. Matter Mater. Phys.*, 2008, **77**, 024112.

42 X. Krokidis, P. Raybaud, A. E. Gobichon, B. Rebours, P. Euzen and H. Toulhoat, Theoretical study of the dehydration process of boehmite to γ-alumina, *J. Phys. Chem. B*, 2001, **105**, 5121–5130.

43 R. Prins, On the structure of γ-Al2O3, *J. Catal.*, 2020, **392**, 336–346.

44 R. Sprycha, Electrical double layer at alumina/electrolyte interface I. Surface charge and zeta potential, *J. Colloid Interface Sci.*, 1989, **127**, 1–11.

45 A. Corma and H. Garci, Supported gold nanoparticles as catalysts for organic reactions, *Chem. Soc. Rev.*, 2008, **37**, 2096–2126.

46 R. Zanella, L. Delannoy and C. Louis, Mechanism of deposition of gold precursors onto TiO2 during the preparation by cation adsorption and deposition-precipitation with NaOH and urea, *Appl. Catal., A*, 2005, **291**, 62–72.

47 O. A. Simakova, V. I. Sobolev, K. Y. Koltunov, B. Campo, A. R. Leino, K. Kordás and D. Y. Murzin, 'Double-Peak' catalytic activity of nanosized gold supported on titania in gas-phase selective oxidation of ethanol, *ChemCatChem*, 2010, **2**, 1535–1538.

48 E. Behravesh, K. Eränen, N. Kumar, J. Peltonen, M. Peurla, A. Aho, M. Nurmi, M. Toivakka, D. Y. Murzin and T. Salmi, Microreactor coating with Au/Al2O3 catalyst for gas-phase partial oxidation of ethanol: Physico-chemical characterization and evaluation of catalytic properties, *Chem. Eng. J.*, 2019, **378**, 122179.

49 J. Rai Jain and C. N. Pillait, Catalytic dehydration of alcohols over alumina mechanism of ether formation, *J. Catal.*, 1967, **9**, 322–330.

50 E. Behravesh, T. Kilpiö, V. Russo, K. Eränen and T. Salmi, Experimental and modelling study of partial oxidation of ethanol in a micro-reactor using gold nanoparticles as the catalyst, *Chem. Eng. Sci.*, 2018, **176**, 421–428.

51 G. R. Jenness, M. A. Christiansen, S. Caratzoulas, D. G. Vlachos and R. J. Gorte, Site-dependent Lewis acidity of γ-Al2O3 and its impact on ethanol dehydration and etherification, *J. Phys. Chem. C*, 2014, **118**, 12899–12907.

52 T. K. Phung and G. Busca, Ethanol dehydration on silica-aluminas: Active sites and ethylene/diethyl ether selectivities, *Catal. Commun.*, 2015, **68**, 110–115.

53 X. Carrier, E. Marceau, J. F. Lambert and M. Che, Transformations of γ-alumina in aqueous suspensions. 1. Alumina chemical weathering studied as a function of pH, *J. Colloid Interface Sci.*, 2007, **308**, 429–437.